STABILITY ESTIMATES FOR RADIAL BASIS FUNCTION METHODS APPLIED TO TIME-DEPENDENT HYPERBOLIC PDES

IGOR TOMINEC*, MURTAZO NAZAROV*, AND ELISABETH LARSSON*

Abstract. We derive stability estimates for three commonly used radial basis function (RBF) methods to solve hyperbolic time-dependent PDEs: the RBF generated finite difference (RBF-FD) method, the RBF partition of unity method (RBF-PUM) and Kansa's (global) RBF method. We give the estimates in the discrete ℓ_2 -norm intrinsic to each of the three methods. The results show that Kansa's method and RBF-PUM can be ℓ_2 -stable in time under a sufficiently large oversampling of the discretized system of equations. On the other hand, the RBF-FD method is not ℓ_2 -stable by construction, no matter how large the oversampling is. We show that this is due to the jumps (discontinuities) in the RBF-FD cardinal basis functions. We also provide a stabilization of the RBF-FD method that penalizes the spurious jumps. Numerical experiments show an agreement with our theoretical observations.

1. Introduction. We explore the theory behind the stability properties of commonly used radial basis function (RBF) methods, when they are used to solve a family of conservation laws:

(1.1)
$$\partial_t u = -\nabla \cdot \mathbf{F}(u) \\ = -\mathbf{F}'(u) \cdot \nabla u,$$

with appropriate initial and inflow boundary conditions, where $u = u(y,t) \in C^k$, k > 0, is a scalar solution function, $y \in \Omega \subset \mathbb{R}^2$, Ω is an open and bounded domain, t is a position in time, $\mathbf{F} = \mathbf{F}(u,t) \in C^1(\mathbb{R}^2)$ is the physical flux and $\mathbf{F}' = \mathbf{F}'(u,t) = \frac{\partial \mathbf{F}(u)}{\partial u}$ is the velocity field. In this work we focus on cases where u is continuous, and where \mathbf{F} is linear, and \mathbf{F}' is divergence-free $\nabla \cdot \mathbf{F}' = 0$. All these constraints give a sufficient setting to understand the L_2 -stability of the numerical solution in time. To have L_2 -stability is also a necessary condition for overall stability when \mathbf{F} is nonlinear and the solution u is discontinuous.

The RBF methods that we investigate are: the RBF generated finite difference (RBF-FD) method [21, 7], the RBF partition of unity method (RBF-PUM) [29] and Kansa's method [11]. The first two methods are localized such that the final system of equations is sparse, and the third method is global and gives a dense system of equations. It is known, based on numerical experiments, that all three methods in general are unstable when computing collocated solutions to time-dependent conservation laws without additional stabilization [8, 1, 22]. Stabilizations, mostly based on supplementing the numerical scheme by a hyperviscosity term, have been studied in [16, 19, 8]. In [6] the authors provide analysis of the oversampled Kansa's method for a parabolic PDE problem on a smooth surface. In [17] the authors utilize a semi-Lagrangian formulation of Kansa's method, RBF-PUM and the RBF-FD method to provide stable numerical solutions of a linear transport problem over the surface of the sphere. In [18] the authors extend the same idea to an overlapped RBF-FD method [15] for linear advection-diffusion problems in 2D. In [12] the authors provided a set of numerical experiments which indicate that Kansa's method applied to (1.1) becomes stable in time when the system of equations is oversampled instead of collocated. Recently, we provided numerical experiments in [26] showing that the RBF-FD method is generally unstable in time, both in the oversampled and in the collocated con-

^{*}Uppsala University, Department of Information Technology, SE-751 05 Uppsala, Sweden. (igor.tominec@it.uu.se, murtazo.nazarov@it.uu.se, elisabeth.larsson@it.uu.se).

text. Our main goal is to get a better understanding of these differences by deriving semi-discrete stability estimates for all three methods, in the sense:

(1.2)
$$\partial_t ||u_h||_{\ell_2}^2 \le \text{boundary data},$$

where $||u_h||_{\ell_2}^2$ is the energy of the numerical solution u_h , measured in the discrete norm $||\cdot||_{\ell_2}$ intrinsic to collocated and oversampled discretizations. When (1.2) contains terms that are not related to the boundary condition data, then $||u_h||_{\ell_2}^2$ has a spurious growth in time leading to an unstable discretization.

A related work is [25] where we introduced an oversampled version of the RBF-FD method for an elliptic model problem, and made a theoretical investigation of its stability properties, where we showed that the RBF-FD method generates a discontinuous trial space and that oversampling of a stationary problem approximates a variational formulation using a least-squares projection. The oversampled RBF-FD method was then also extended to an unfitted setting in [24], which was later used for the simulations of a thoracic diaphragm in [27]. In [26] we introduced the oversampled RBF-FD method to solve nonlinear conservation laws with discontinuous solutions, and found that oversampling approximates a strong variational formulation using a Galerkin projection, but the method is still unstable in time. In the same paper we used a hyperviscosity stabilization in time and the residual viscosity stabilization from [13] to stabilize the discontinuous solutions. In [9, 10] the authors have derived stability estimates for time-dependent linear conservation laws, discretized using a Kansa-type method that employs a weak variational form through exact integration, and outlined that the boundary conditions have to be imposed weakly for the method to be stable.

The main contributions of the present work are: (a) Kansa's method and RBF-PUM can be stable in time under a sufficient amount of oversampling, (b) the RBF-FD method is generally unstable in time due to its discontinuous trial space (jumps in the cardinal basis functions), (c) the RBF-FD method can be stabilized by forcing the jump term over the interfaces of the discontinuities towards 0, (d) strong imposition of the inflow boundary conditions is in practice not preventing Kansa's method, RBF-PUM or the stabilized RBF-FD method from being stable in time.

The paper is organized as follows: in Section 2 we discretize the nonlinear conservation law (1.1) in an oversampled context, when the numerical solution is spanned by a set of global cardinal functions. Then we discuss how to construct the global cardinal basis function by three different methods: in Section 3 we formulate Kansa's method (i), in Section 4 we formulate RBF-PUM (ii), in Section 5 we formulate the RBF-FD method (iii). Then in Section 6 we derive semi-discrete stability estimates of type (1.2) for each method, provide the interpretation and propose an alternative, jump-based stabilization of the RBF-FD method. In Section 7 we validate the theoretical results by computing the eigenvalue spectra of the discretized advection operators for (i), (ii) and (iii) and show the numerical convergence results when solving (1.1), as well as the stability properties during a long-time simulation. We make a final discussion in Section 8.

2. Collocation and oversampled discretization of a time-dependent linear advection problem. Here we discretize the linear advection problem (1.1) in a collocated and an oversampled sense.

The domain Ω on which we solve (1.1) is discretized using two point sets:

- the nodal point set X = {x_i}_{i=1}^N for generating the cardinal basis functions,
 the evaluation point set Y = {y_j}_{j=1}^M for sampling the PDE (1.1), where

$$M = qN$$
.

An example of two point sets is visualized in Figure 2.1. In the present work, we generate the X point set such that the mean distance between the points is set to h, by using the DistMesh algorithm [14], which is in some cases randomly perturbed to also generalize the numerical results to less regular set of points. When using the oversampled discretization, the Y point set is also generated by DistMesh, but with an internodal distance $h_y = \frac{h}{\sqrt{q}}$. When using the collocation discretization we set Y = X, where, as a consequence we have that $h = h_y$. We note that for a given point set $Y \subset \mathbb{R}^d$, we can define $h_y = (\frac{|\Omega|}{M})^{1/d}$. Here $|\Omega|$ is a d-dimensional volume of Ω , which can be estimated by $\Omega = \tilde{M} \frac{|\Omega_c|}{M_c}$, where Ω_c is a d-dimensional box that encapsulates Ω , M_c is the number of points inside Ω_c and \tilde{M} is the number of points in $\Omega_c \cap \Omega$.

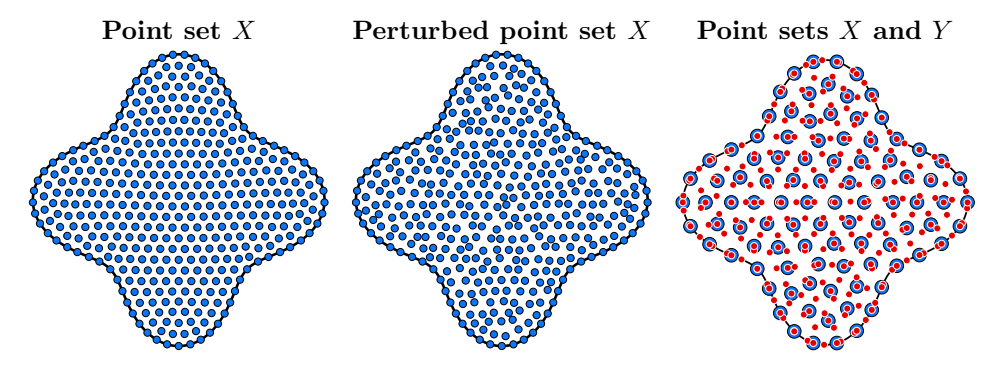


Fig. 2.1: Plots from left to right: a point set X (blue markers) obtained using DistMesh, a randomly perturbed DistMesh X point set (blue markers), point set X (blue markers) together with the evaluation point set Y (red markers), where the oversampling parameter is set to q=4.

To evaluate the RBF solution and its derivatives for any of the methods, we use:

(2.1)
$$u_h(y,t) = \sum_{i=1}^{N} u_h(x_i,t)\Psi_i(y), \quad \mathcal{L}u_h(y,t) = \sum_{i=1}^{N} u_h(x_i,t)\mathcal{L}\Psi_i(y),$$

where $\Psi_i(y)$ i=1,...,N are the cardinal basis functions that together interpolate the unknown nodal values $u_h(x_i,t)$. The cardinal basis functions are constructed differently and have different mathematical properties, depending on the choice of the RBF method as shown in the sections below.

The discretization of (1.1) is based on inserting the ansatz (2.1) into (1.1) and then sampling the PDE at the evaluation point set as follows:

$$(2.2) \sum_{i=1}^{N} \partial_t u_h(x_i, t) \Psi_i(y_k) = -F_1' \sum_{i=1}^{N} u_h(x_i, t) \nabla_1 \Psi_i(y_k) - F_2' \sum_{i=1}^{N} u_h(x_i, t) \nabla_2 \Psi_i(y_k),$$

$$k = 1, \dots, M.$$

Here ∇_j , j = 1, 2 is the first derivative in the j-th coordinate of y, and F'_1, F'_2 depend on time t. We rewrite (2.2) on the matrix-vector format as:

$$(2.3) E_h \partial_t u_h(X, t) = D_h u_h(X, t),$$

where $(E_h)_{ki} = \Psi_i(y_k)$ and $(D_h)_{ki} = -F_1'\nabla_1\Psi_i(y_k) - F_2'\nabla_2\Psi_i(y_k)$. When M = N in (2.2), then the discretization is performed in the collocation sense and the matrices E_h and D_h in (2.3) are square. When M > N, the discretization is oversampled: E_h and D_h are rectangular. In order to simplify the theoretical analysis at a later stage in this paper, we introduce a norm scaling of (2.3) for a 2D problem [25], and define $\bar{E}_h = h_y E_h$ and $\bar{D}_h = h_y D_h$, to obtain:

$$(2.4) \bar{E}_h \partial_t u_h(X, t) = \bar{D}_h u_h(X, t),$$

Since the matrices in (2.4) in general are rectangular we require a projection onto a certain column space in order to rewrite (2.4) so that the resulting system of ODEs can be advanced in time. We project (2.4) onto the column space of E_h by multiplying both sides of the PDE by E_h^T :

$$(2.5) \qquad (\bar{E}_h^T \bar{E}_h) \, \partial_t u_h(X, t) = (\bar{E}_h^T \bar{D}_h) \, u_h(X, t),$$

The components of the matrix products involved in (2.5) are:

$$(2.6) (\bar{E}_h^T \bar{E}_h)_{ij} = (\Psi_i, \Psi_j)_{\ell_2}, (\bar{E}_h^T \bar{D}_h)_{ij} = -(\Psi_i, \mathbf{F}' \cdot \nabla \Psi_j)_{\ell_2},$$

where $(u,v)_{\ell_2} = h_y^2 \sum_{k=1}^M u(y_k) \, v(y_k)$ is a discrete inner product. The ℓ_2 inner product is an approximation of the L_2 inner product $(u,v)_{L_2} = \int_{\Omega} uv \, d\Omega$ [25]. Interestingly, if we had initially projected (1.1) using the L_2 inner product, instead of employing oversampling and a projection that led to the ℓ_2 inner product, the final discretization would have yielded a pure Galerkin scheme. Finally, the system of ODEs is obtained from (2.5) by inverting $\bar{E}_b^T \bar{E}_b$:

(2.7)
$$\partial_t u_h(X,t) = (\bar{E}_h^T \bar{E}_h)^{-1} (\bar{E}_h^T \bar{D}_h) u_h(X,t).$$

In practice, we do not invert $(\bar{E}_h^T \bar{E}_h)$ directly, but instead use an iterative solver for (2.5) in each step of an explicit time-stepping algorithm. Since $(\bar{E}_h^T \bar{E}_h)$ is symmetric and typically well conditioned, we use the conjugate gradient method (function pcg() in MATLAB).

In this work we consider the problem (1.1) with a Dirichlet boundary condition specified on the inflow part of $\partial\Omega$. The boundary conditions in (2.7) are imposed in two ways: (i) when studying the eigenvalue spectra in the experimental part of this paper, we remove the values of the vector $u_h(X,t)$ located on the inflow boundary, together with the corresponding columns and rows in the matrices, (ii) when computing the numerical solution in time, we impose the condition using the injection method, that is, we overwrite the solution $u_h(X,t_i)$, i=1,2,... with the corresponding inflow boundary value, after each step of the explicit time-stepping algorithm. The procedures (i) and (ii) are equivalent.

3. Kansa's global RBF method. We work with a global interpolant defined on Ω , where the interpolant is exact for radial basis functions $\phi_l(x)$, l = 1, ..., N and the monomial basis, $\bar{p}_k(x)$, k = 1, ..., m. The interpolant is:

(3.1)
$$u_h(x,t) = \sum_{l=1}^{N} c_l(t)\phi_l(x) + \sum_{k=1}^{m} \beta_k(t)\bar{p}_k(x),$$
 subject to
$$\sum_{l=1}^{N} c_l(t)\bar{p}_k(x_l) = 0, \quad k = 1,..,m,$$

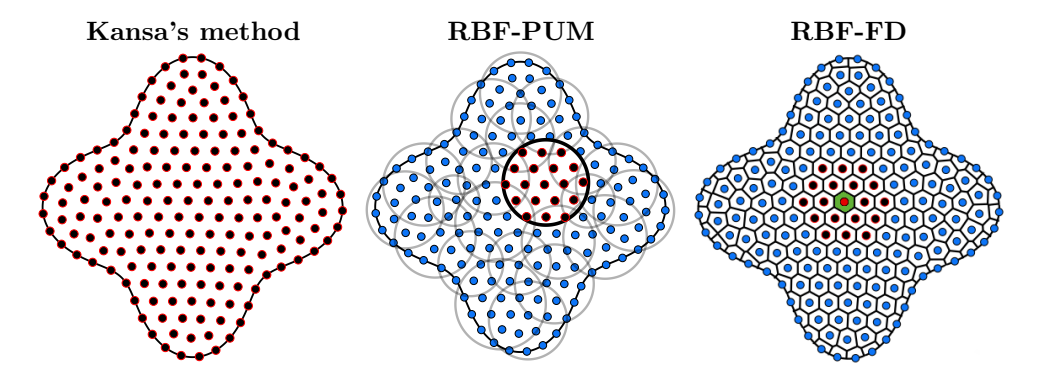


Fig. 3.1: Nodes (blue points) and different node supports (black points with red edges) specific to three RBF methods: Kansa's RBF method (global support), the RBF partition of unity method (patch support) and the RBF generated finite difference (RBF-FD) method (stencil support). The green area in the RBF-FD method case illustrates the region to which the stencil approximation is further restricted when evaluating the numerical solution.

where $c_l(t)$ are the unknown interpolation coefficients, $\beta_k(t)$ the unknown Lagrange multipliers, and where the number of monomial terms is $m = \binom{D_m+2}{2}$, where D_m is the degree of the monomial basis. The discussion in this paper applies for any RBF, however, in our computations we use the cubic polyharmonic spline (PHS) basis $\phi_l(x) = ||x - x_l||_2^3$. PHS and the monomial basis as a combination, were introduced and studied in [2, 3, 4]. In (3.1) the objective is now to determine the interpolation coefficients c_l and the Lagrange multipliers β_k , by requiring the interpolation conditions $u_h(x_i, t) = u(x_i, t)$, i = 1, ..., N, where $x_i \in X$ and $u(x_i, t)$ are the unknown nodal values to be fulfilled. The result is a system of equations in matrix-vector format:

$$(3.2) \qquad \underbrace{\begin{pmatrix} A & P \\ P^T & 0 \end{pmatrix}}_{:-\tilde{A}} \left(\underline{\underline{c}(t)} \right) = \begin{pmatrix} \underline{u}(X,t) \\ 0 \end{pmatrix} \quad \Leftrightarrow \quad \left(\underline{\underline{c}(t)} \right) = \tilde{A}^{-1} \begin{pmatrix} \underline{u}(X,t) \\ 0 \end{pmatrix}.$$

Here $A_{jl} = \phi_l(x_j)$ for indices j, l = 1, ..., N and $P_{jk} = \bar{p}_k(x_j)$ for indices k = 1, ..., m and $u_j = u(x_j, t)$. The solution $u_h(y), y \in \Omega$, is then written by reusing the computed coefficients inside (3.1) and only keeping the first N terms, and disregarding the N + 1, ..., N + m terms which are related to the Lagrange multipliers:

$$(3.3) u_h(y,t) = \underbrace{\left(\phi_1(y), ..., \phi_N(y), \bar{p}_1(y), ..., \bar{p}_m(y)\right)}_{:=b(y)} \underbrace{\left(\frac{c(t)}{\beta(t)}\right)}_{0} = \left(b(y)\tilde{A}^{-1}\right)_{1:N} \underline{u}(X,t)$$

$$= \sum_{k=1}^{N} u(x_k, t) \left[b(y, X) \tilde{A}^{-1}(X, X)\right]_k \equiv \sum_{k=1}^{N} u(x_k, t) \Psi_k(y)$$

Here we also derived a vector, continuous in y, of cardinal basis functions $\Psi_1(y), ..., \Psi_N(y)$ used to construct $u_h(y, t)$ in (2.1). For Kansa's method, the matrices of the discretization (2.4) are dense.

4. The RBF partition of unity method (RBF-PUM). As for Kansa's method, the domain Ω is first discretized using the nodal points X. Then we construct an open cover of Ω using the patches $\Omega^{(j)}$, $j=1,...,N_p$, such that $\Omega\subset \cup_{i=1}^{N_p}\Omega^{(j)}$. Each patch contains $n^{(j)}\geq 2\binom{D_m+2}{2}$ points, where the points of the j-th patch are denoted by $X^{(j)}\subset X$. The RBF-PUM solution is represented as follows. We form an interpolant on $\Omega^{(j)}$ analogously to Kansa's method on the whole Ω : we use (2.1) that leads to (3.3), where N is replaced by $n^{(j)}$, and X by $X^{(j)}$. The result is a local solution:

$$(4.1) \quad u_h^{(j)}(y,t) = \sum_{k=1}^{n^{(j)}} u(x_k^{(j)},t) \left[b(y,X^{(j)}) \, \tilde{A}^{-1}(X^{(j)},X^{(j)}) \right]_k \equiv \sum_{k=1}^{n^{(j)}} u(x_k^{(j)},t) \psi_k^{(j)}(y),$$

where $\psi_k^{(j)}(y)$ are now the local RBF-PUM cardinal functions. Then the global solution $u_h \in \Omega$ is defined by blending $u_h^{(j)}$ together using compactly supported weight functions $w_i(y)$ such that:

$$(4.2) u_h(y,t) = \sum_{j=1}^{N_p} w_j(y) u_h^{(j)}(y,t) = \sum_{j=1}^{N_p} w_j(y) \sum_{k=1}^{n^{(j)}} u(x_k^{(j)}, t) \psi_k^{(j)}(y),$$

where each $w_j(y)$ is constructed using Shepard's method [20]: (4.3)

$$w_j(y) = \frac{\Phi_j(y)}{\sum_{i=1}^{N_p} \Phi_i(y)}, \quad \Phi_j(y) = (4r_j + 1)(1 - r_j^4)_+, \quad r_j = \frac{\|y - \xi_j\|_2}{R_j}, \quad j = 1, ..., N_p.$$

Here Φ_j are chosen as $C^2(\Omega)$ Wendland functions [28] with compact support on $\Omega^{(j)}$, and ξ_j and $R_j > 0$ are consecutively the center and the radius of $\Omega^{(j)}$. The global solution (4.2) is now cast in an equivalent form that is analogous to (2.1), by introducing: (a) a set J(i) of all patches where x_i is contained, (b) an index operator $\kappa(j,i)$, which gives the local index of x_i inside a patch $\Omega^{(j)}$. We then have:

$$(4.4) u_h(y,t) = \sum_{j=1}^{N_p} w_j(y) \sum_{k=1}^{n^{(j)}} u(x_k^{(j)}, t) \psi_k^{(j)}(y)$$

$$= \sum_{i=1}^N u_h(x_i, t) \sum_{j \in J(i)} w_j(y) \psi_{\kappa(j,i)}^{(j)}(y) \equiv \sum_{i=1}^N u_h(x_i, t) \Psi_i(y).$$

and thus $\Psi_i(y) = \sum_{j \in J(i)} w_j(y) \psi_{\kappa(j,i)}^{(j)}(y)$. By using the RBF-PUM cardinal basis functions $\Psi_i(y)$ to discretize a time-dependent PDE as in (2.2), the involved matrices in (2.4) become sparse.

5. The RBF generated finite difference (RBF-FD) method. The domain Ω is discretized using the nodal points X. Then we form a stencil for each $x_i \in X$, based on the $n = 2\binom{D_m+2}{2}$ nearest neighbors, where each stencil is represented with a point set $X^{(j)} \subset X$, j = 1,..,N. On each stencil point set $X^{(j)}$ we form a local interpolation problem by using (2.1) that leads to (3.3), where N is replaced by n, and X by $X^{(j)}$. The result is a set of stencil based approximations:

$$(5.1) \quad u_h^{(j)}(y,t) = \sum_{k=1}^n u(x_k^{(j)},t) \left[b(y,X^{(j)}) \tilde{A}^{-1}(X^{(j)},X^{(j)}) \right]_k \equiv \sum_{k=1}^n u(x_k^{(j)},t) \psi_k^{(j)}(y),$$

$$j = 1,...,N,$$

where $\psi_k^{(j)}(y)$ are the local RBF-FD cardinal functions. To arrive at the global solution $u_h(y) \in \Omega$ we first associate every y with the index of the closest stencil center point defined as:

(5.2)
$$\rho(y) = \arg\min_{i \in [1, N]} ||y - x_i||_2.$$

Analogously to the situation in RBF-PUM (4.2) we write the global solution as:

(5.3)
$$u_h(y,t) = u_h^{(\rho(y))}(y,t) = \sum_{k=1}^n u(x_k^{(\rho(y))}, t) \psi_k^{(\rho(y))}(y).$$

This implies that each $u_h(y)$ in a Voronoi region centered around $x_{\rho(y)} \in X$ is represented by a local solution $u_h^{\rho(y)}(y,t)$. An equivalent form of (5.3) that is analogous to (2.1) is written by using an index operator $\kappa(\rho(y),i)$ which in the RBF-FD method case gives the local index of x_i inside a stencil point set $X^{(\rho(y))}$.

(5.4)
$$u_h(y,t) = \sum_{k=1}^n u(x_k^{(\rho(y))}, t) \, \psi_k^{(\rho(y))}(y)$$
$$= \sum_{i=1}^N u(x_i, t) \, \psi_{\kappa(\rho(y), i)}^{(\rho(y))}(y) \equiv \sum_{i=1}^N u(x_i, t) \Psi_i(y).$$

The global RBF-FD cardinal functions are thus $\Psi_i(y) = \psi_{\kappa(\rho(y),i)}^{(\rho(y))}(y)$. In this case we do not have any blending weight functions that ensure the continuity across the Voronoi regions, as is the case for RBF-PUM (see (4.4)), and thus the RBF-FD global solution is discontinuous across the edges between these regions. Even if each $u_h^{(\rho(y))} \in C^2$ in one stencil, due to the properties of the local cardinal basis functions, we only have that $u_h \in L_2(\Omega)$. A visualization of the discontinuities (jumps) in one RBF-FD cardinal basis function is given in [25, Figure 2].

A MATLAB code for obtaining the collocated or the oversampled RBF-FD matrices is available from [23].

- 6. Stability properties of RBF methods for linear advection problems. We derive semi-discrete stability estimates of type (1.2) for the PDE discretization given in (2.2), where the cardinal basis functions Ψ_i , i = 1, ..., N are constructed using three RBF methods: Kansa's method described in Section 3, RBF-PUM described in Section 4 and the RBF-FD method described in Section 5.
- **6.1. Definitions of the inner products and norms.** To measure the stability, we define a discrete inner product for functions u_h , v_h sampled at Y-points:

$$(u_h(Y,t), v_h(Y,t))_{\ell_2(\Omega)} = (\bar{E}u_h(X,t), \bar{E}v_h(X,t))_{\ell_2(\Omega)}$$

$$= u_h^T(X,t)\bar{E}^T\bar{E}v_h(X,t) = h_y^2 \sum_{j=1}^M u_h(y_j,t) v_h(y_j,t),$$
(6.1)

where \bar{E} is defined in the scope of (2.4) and h_y in Section 2. The induced discrete norm is then:

(6.2)
$$(u_h(Y,t), u_h(Y,t))_{\ell_2(\Omega)} = u_h^T(X,t)\bar{E}^T\bar{E}\,u_h(X,t) = \|u_h(Y,t)\|_{\ell_2(\Omega)}^2.$$

A link between our discretization and the chosen inner product is described in Section 2. The stability estimates derived later in this section are based on a relation between the ℓ_2 inner product and the L_2 inner product. The latter is defined by:

$$(6.3) (u_h(y,t), v_h(y,t))_{L_2(\Omega)} = \int_{\Omega} u_h(y,t) v_h(y,t) d\Omega, \quad y \in \Omega,$$

We use the integration error estimate (A.2) derived in Appendix A, to relate the two inner products as:

(6.4)
$$(u_h, v_h)_{\ell_2(\Omega)} \leq C_{\int} h^{-1} h_y \max_{ij} \|u_h v_h\|_{L_{\infty}(K_{ij})} + (u_h, v_h)_{L_2(\Omega)}$$
$$\equiv e_I(u_h, v_h) + (u_h, v_h)_{L_2(\Omega)}.$$

where C_f is independent of h_y and h. We have that for a fixed h, the integration error approaches 0 as $h_y \to 0$. The integration error estimate is later also numerically validated in Section 7.1.

6.2. A semi-discrete stability estimate for Kansa's RBF method. Consider a numerical solution u_h spanned by the cardinal basis functions defined in (3.3). Observe that the regularity of u_h is given by the lowest regularity of the bases ϕ_l and \bar{p}_k used in (3.3). This implies $\Psi_i \in C^2(\Omega)$ and $u_h \in C^2(\Omega)$. The derivation that follows is based on that regularity fact, since we are then allowed to differentiate the solution u_h over the whole Ω .

We consider the discrete problem (2.5) and multiply it with $u_h^T(X,t)$:

(6.5)
$$u_h^T(X,t)\bar{E}_h^T\bar{E}_h\,\partial_t u_h(X,t) = u_h^T(X,t)\bar{E}_h^T\bar{D}_h\,u_h(X,t).$$

Using the relation (6.1) for both sides of (6.5) and using (2.6) for the right-hand-side of (6.5), we rewrite (6.5) on the form:

$$(6.6) (u_h(Y,t), \partial_t u_h(Y,t))_{\ell_2(\Omega)} = -(u_h(Y,t), F' \cdot \nabla u_h(Y,t))_{\ell_2(\Omega)}.$$

Now we use an identity: $(u_h(Y,t), \partial_t u_h(Y,t))_{\ell_2(\Omega)} = \frac{1}{2}\partial_t (u_h(Y,t), u_h(Y,t))_{\ell_2(\Omega)} = \frac{1}{2}\partial_t ||u_h(Y,t)||_{\ell_2}^2$ on the left-hand-side of (6.6) and the inequality (6.4) on the right-hand side of (6.6) to obtain:

(6.7)
$$\frac{1}{2}\partial_t \|u_h\|_{\ell_2(\Omega)}^2 \le e_I(u_h(F' \cdot \nabla u_h)) - (u_h, F' \cdot \nabla u_h)_{L_2(\Omega)},$$

where e_I is the integration error and where we also dropped the (Y,t) notation for simplicity. The inner product on the right-hand-side of (6.7) is well known to be skew-symmetric, which, provided that $\nabla \cdot F' = 0$, implies that $(u_h, F' \cdot \nabla u_h)_{L_2(\Omega)} = \frac{1}{2} \int_{\partial \Omega} u_h^2 F' \cdot n \, ds$, where n is the outward normal of Ω . Using that in (6.7) and multiplying the resulting inequality by 2 we obtain:

(6.8)
$$\partial_t \|u_h\|_{\ell_2(\Omega)}^2 \le 2 e_I(u_h(F' \cdot \nabla u_h)) - 2 \int_{\partial \Omega} u_h^2 F' \cdot n \, ds.$$

We split the boundary $\partial\Omega$ into an inflow and an outflow part such that $\Omega = \Gamma_{\rm inflow} \cup \Gamma_{\rm outflow}$. The two parts are defined as:

$$(6.9) \qquad \Gamma_{\rm inflow} := \{ y \in \partial \Omega \, | \, F' \cdot n < 0 \}, \quad \Gamma_{\rm outflow} := \{ y \in \partial \Omega \, | \, F' \cdot n \geq 0 \}.$$

The boundary integral in (6.8) is split into a sum:

$$-2\int_{\partial\Omega}u_h^2\,F'\cdot n\,ds = -2\int_{\Gamma_{\rm inflow}}u_h^2\,F'\cdot n\,ds - 2\int_{\Gamma_{\rm outflow}}u_h^2\,F'\cdot n\,ds,$$

and then by using the sign of $F' \cdot n$ from (6.9) we bound $-2 \int_{\Gamma_{\text{inflow}}} u_h^2 F' \cdot n \, ds \le 2 \int_{\Gamma_{\text{inflow}}} u_h^2 |F' \cdot n| \, ds$ and $-2 \int_{\Gamma_{\text{outflow}}} u_h^2 F' \cdot n \, ds \le 0$. Using these two bounds in (6.8) and (6.4) to define the e_I term, we obtain the final semi-discrete stability estimate: (6.10)

$$\begin{aligned} \partial_t \|u_h\|_{\ell_2(\Omega)}^2 &\leq 2 \, C_{\int} \, h^{-1} h_y \max_{ij} \|u_h(F' \cdot \nabla u_h)\|_{L_{\infty}(K_{ij})} + 2 \int_{\Gamma_{\text{inflow}}} u_h^2 \, |F' \cdot n| \, ds \\ &\leq C h^{-2} h_y \max_{ij} \|F'\|_{L_{\infty}(K_{ij})} \|u_h\|_{L_{\infty}(K_{ij})}^2 + 2 \int_{\Gamma_{\text{inflow}}} u_h^2 \, |F' \cdot n| \, ds, \end{aligned}$$

where we also used an inverse inequality $\|\nabla u_h\|_{L_{\infty}(K_{ij})} \leq C_I \|u_h\|_{L_{\infty}(K_{ij})}$, and defined $C = 2C_{\int}C_I$. Thus, Kansa's RBF method has a solution of which the discrete norm is bounded in time by the inflow boundary term, and an integration error term of which the magnitude is possible to control by decreasing h_y when h is fixed.

- 6.3. A semi-discrete stability estimate for RBF-PUM. The RBF-PUM solution u_h defined in (4.2) and (4.4) is $C^2(\Omega)$, since the subproblems defined on the patches are $C^2(\Omega_j)$, $j = 1,...,N_p$, which are then blended together using the partition of unity weight functions $w_j \in C^2(\Omega)$. The semi-discrete stability estimate is then precisely the same as for Kansa's RBF method stated in (6.10), since the only assumption to derive it, was a sufficient regularity of the global solution and a sufficient amount of oversampling used to discretize the PDE.
- 6.4. A semi-discrete stability estimate for the RBF-FD method. In the RBF-FD case we are dealing with a function space spanned using a set of discontinuous global cardinal functions. For that reason we can not globally differentiate the solution over Ω and can therefore not inherit the stability result from the derivation for Kansa's RBF method in Section 6.2. However, we instead employ piecewise differentiation and make an estimate using similar techniques as in Kansa's method. We first define a Voronoi region K_i as:

(6.11)
$$K_i = \{ y \in \Omega \mid ||y - x_i|| \le ||y - x_j||, \ j \ne i, \ j = 1, ..., N \}, \quad i = 1, ..., N,$$

and further note that $\bigcup_{i=1}^{N} K_i = \Omega$. We start to make an estimate as in (6.6), but restrict the inner products to K_i :

$$(6.12) (u_h(Y,t), \partial_t u_h(Y,t))_{\ell_2(K_i)} = -(u_h(Y,t), F' \cdot \nabla u_h(Y,t))_{\ell_2(K_i)}, \quad i = 1, ..., N.$$

We first sum the equation above over all K_i and rewrite the left-hand-side term in terms of Ω by using that $\bigcup_{i=1}^{N} K_i = \Omega$. We have:

(6.13)
$$(u_h, \partial_t u_h)_{\ell_2(\Omega)} = \sum_{i=1}^N -(u_h, F' \cdot \nabla u_h)_{\ell_2(K_i)},$$

where we also dropped the (Y,t) notation. Just as in (6.7) we rewrite (6.13) so that we obtain the time derivative of a norm on the left, and use the inequality (6.4) for the integration error of piecewise continuous functions on the right, and obtain:

(6.14)
$$\partial_t \|u_h\|_{\ell_2(\Omega)}^2 \le 2 e_I(u_h(F' \cdot \nabla u_h)) - 2 \sum_{i=1}^N (u_h, F' \cdot \nabla u_h)_{L_2(K_i)},$$

Analogously to (6.8), we now integrate each each inner product by parts on the right side of (6.14), where we also use that $\nabla \cdot F' = 0$, and obtain:

(6.15)
$$\partial_t \|u_h\|_{\ell_2(\Omega)}^2 \le 2 e_I(u_h(F' \cdot \nabla u_h)) - 2 \sum_{i=1}^N \int_{\partial K_i} u_h^2 F' \cdot n_{K_i} \, ds,$$

where ∂K_i is the boundary of K_i and n_{K_i} is the outward normal of K_i . Now we take care of the Voronoi boundary terms on the right of (6.15) by noting that each ∂K_i is made of connected Voronoi edges. Furthermore, some ∂K_i are contained inside Ω and some on $\partial \Omega$. This implies that two neighboring interior Voronoi cells always share an edge, where each cell has an opposite normal direction. Let us first define the set of all interior Voronoi edges as $\mathcal{E}^I = \mathcal{E}^I_+ \cup \mathcal{E}^I_-$, where \mathcal{E}^I_+ are the interior edges with a positive normal direction n^+ and \mathcal{E}^I_- the interior edges with a negative normal direction n^- . The two normal directions are defined analogously to (6.9) as:

(6.16)
$$n_{K_i}^- = \{n|_{\partial K_i} : F' \cdot n < 0\}, \quad n_{K_i}^+ = \{n|_{\partial K_i} : F' \cdot n \ge 0\}.$$

Then the sum on the right hand side of (6.15) is rewritten in terms of \mathcal{E}^I and $\partial\Omega$: (6.17)

$$\partial_t \|u_h\|_{\ell_2(\Omega)}^2 \le 2 e_I(u_h(F' \cdot \nabla u_h)) - 2 \Big[\int_{\partial \Omega} u_h^2 F' \cdot n \, ds + \Big]$$

$$+ \sum_{\mathcal{E}_i \in \mathcal{E}^I} \int_{\mathcal{E}_i} \left((u_h^+)^2 F' \cdot n_{\mathcal{E}_i}^+ + (u_h^-)^2 F' \cdot n_{\mathcal{E}_i}^- \right) \, ds \Big].$$

The positive and the negative normals along the same edge \mathcal{E}_i are related by $n_{\mathcal{E}_i}^- = -n_{\mathcal{E}_i}^+$. Further, we split the integral over $\partial\Omega$ in the inflow part $\Gamma_{\rm inflow}$ and the outflow part $\Gamma_{\rm outflow}$, both defined in (6.9) such that $\int_{\partial\Omega}u_h^2\,F'\cdot n\,ds=\int_{\Gamma_{\rm inflow}}u_h^2\,F'\cdot n\,ds+\int_{\Gamma_{\rm outflow}}u_h^2\,F'\cdot n\,ds$. We obtain: (6.18)

$$\begin{aligned} \partial_t \|u_h\|_{\ell_2(\Omega)}^2 \leq & 2 \, e_I(u_h(F' \cdot \nabla u_h)) - 2 \Big[\int_{\Gamma_{\text{inflow}}} u_h^2 \, F' \cdot n \, ds + \int_{\Gamma_{\text{outflow}}} u_h^2 \, F' \cdot n \, ds + \\ & + \sum_{\mathcal{E}_i \in \mathcal{E}^I} \int_{\mathcal{E}_i} \left[(u_h^+)^2 - (u_h^-)^2 \right] \, F' \cdot n_{\mathcal{E}_i}^+ \, ds \Big]. \end{aligned}$$

In the same way as in Section 6.2, we now use the sign of $F' \cdot n$ from (6.9) to further bound (6.18) by using $-\int_{\Gamma_{\text{inflow}}} u_h^2 F' \cdot n \, ds \leq \int_{\Gamma_{\text{inflow}}} u_h^2 |F' \cdot n| \, ds$ and $-\int_{\Gamma_{\text{outflow}}} u_h^2 F' \cdot n \, ds \leq 0$, and we also use (6.4) to define the e_I term, and arrive to: (6.19)

$$\begin{split} \partial_t &\|u_h\|_{\ell_2(\Omega)}^2 \leq 2 \, C_{\int} \, h^{-1} h_y \max_{ij} \|u_h(F' \cdot \nabla u_h)\|_{L_{\infty}(K_{ij})} + \\ &+ 2 \Big[\int_{\Gamma_{\text{inflow}}} u_h^2 \, |F' \cdot n| \, ds \, - \sum_{\mathcal{E}_i \in \mathcal{E}^I} \int_{\mathcal{E}_i} \left[(u_h^+)^2 - (u_h^-)^2 \right] \, F' \cdot n_{\mathcal{E}_i}^+ \, ds \Big] \\ &\leq 2 \, C h^{-2} h_y \max_{ij} \|F'\|_{L_{\infty}(K_{ij})} \|u_h\|_{L_{\infty}(K_{ij})}^2 + \\ &+ 2 \Big[\int_{\Gamma_{\text{inflow}}} u_h^2 \, |F' \cdot n| \, ds \, - \sum_{\mathcal{E}_i \in \mathcal{E}^I} \int_{\mathcal{E}_i} \left[(u_h^+)^2 - (u_h^-)^2 \right] \, F' \cdot n_{\mathcal{E}_i}^+ \, ds \Big], \end{split}$$

where, we used an inverse inequality in the second step in a similar way as in (6.10), and where we consequently have that $C = 2C_{\int}C_{I}$. This is the finalized semi-discrete

stability estimate for the RBF-FD method with oversampling. From (6.19) we observe that the solution norm is bounded by the inflow boundary term, by the jump term and by the numerical integration term. The latter two terms do not originate from the physical properties of the PDE problem, however, the numerical integration error estimate term is positive and can be made arbitrarily small for a fixed h, by decreasing h_y (increasing the oversampling). The jump term is more problematic because it has an arbitrary sign, and there is no obvious control over it to make it smaller. Our conclusion is that the RBF-FD solution is not guaranteed to be stable in time by construction, without including additional stabilization terms, and that even if we send $h_y \to 0$ (equivalent to employing exact integration), the jump term is still going to prevent the method from being stable.

6.5. Interpretation of the derived semi-discrete stability estimates in the sense of the eigenvalue spectrum of the ODE system. The semi-discrete stability estimate is an upper bound of the real part of the eigenvalues of the ODE matrix $(\bar{E}_h^T \bar{E}_h)^{-1} (\bar{E}_h^T \bar{D}_h)$ in the semi-discrete problem (2.7). To show that, for the sake of clarity, we consider a case where $u_h|_{\Gamma_{\rm inflow}} = 0$ and limit ourselves to Kansa's RBF method and RBF-PUM which do not contain the spurious jump term. The stability estimate (6.10) then simplifies to:

(6.20)
$$\partial_t \|u_h(Y,t)\|_{\ell_2(\Omega)}^2 \le Ch^{-2}h_y \max_{ij} \|F'\|_{L_\infty(K_{ij})} \|u_h\|_{L_\infty(K_{ij})}^2$$

Substituting (6.2) into the left hand side of the estimate above, and then using that $u_h^T \bar{E}_h^T \bar{E}_h u_h \ge u_h^T u_h$ as shown in [25], we have that: (6.21)

$$\partial_t u_h^T u_h \le \partial_t u_h^T \bar{E}_h^T \bar{E}_h u_h = \partial_t \|u_h(Y, t)\|_{\ell_2(\Omega)}^2 \le C h^{-2} h_y \max_{i, i} \|F'\|_{L_\infty(K_{ij})} \|u_h\|_{L_\infty(K_{ij})}^2.$$

Further, we multiply (2.7) by u_h^T and using the chain rule identity $u_h^T \partial_t u_h = \frac{1}{2} \partial_t u_h^T u_h$ on the left-hand-side, we obtain that:

(6.22)
$$\partial_t u_h^T u_h = 2u_h^T (\bar{E}_h^T \bar{E}_h)^{-1} (\bar{E}_h^T \bar{D}_h) u_h.$$

By inserting (6.22) into (6.21) and dividing the resulting inequality by 2 we finally obtain:

$$(6.23) u_h^T (\bar{E}_h^T \bar{E}_h)^{-1} (\bar{E}_h^T \bar{D}_h) u_h \le \frac{1}{2} C h^{-2} h_y \max_{ij} \|F'\|_{L_{\infty}(K_{ij})} \|u_h\|_{L_{\infty}(K_{ij})}^2,$$

from which it follows that:

$$\sup_{\|u_h\|_2=1} u_h^T (\bar{E}_h^T \bar{E}_h)^{-1} (\bar{E}_h^T \bar{D}_h) u_h = \frac{1}{2} C h^{-2} h_y \max_{ij} \|F'\|_{L_{\infty}(K_{ij})} \|u_h\|_{L_{\infty}(K_{ij})}^2$$

$$= \operatorname{Real}(\lambda_{\max}(\bar{E}_h^T \bar{E}_h)^{-1} (\bar{E}_h^T \bar{D}_h)).$$

Thus, the real part of all eigenvalues of the RHS ODE matrix $(\bar{E}_h^T \bar{E}_h)^{-1} (\bar{E}_h^T \bar{D}_h)$ is bounded from above by $\frac{1}{2}Ch^{-2}h_y \max_{ij} \|F'\|_{L_{\infty}(K_{ij})} \|u_h\|_{L_{\infty}(K_{ij})}^2$, and this is the main message of this section. Note that under the assumption of the equivalence $\max_{ij} \|u_h\|_{L_{\infty}(K_{ij})}^2 = \|u_h\|_{\infty}^2$, we have that:

$$||u_h||_{\infty}^2 \le ||u_h||_2^2 = u_h^T E_h^T E_h u_h \le \sup_{||u_h||_0 = 1} u_h^T E_h^T E_h u_h = \lambda_{\max}(E_h^T E_h).$$

6.6. The magnitudes of the spurious jumps in the RBF-FD cardinal functions. An a priori estimate of the magnitude of the jumps in the RBF-FD cardinal basis functions is at the present moment not available. Therefore we investigate these jumps numerically. For simplicity, we focus on a 1D case, where Ω is the interval [0, 1]. The objective is to understand the behavior of the discontinuities present in the RBF-FD trial space as a function of the stencil size n, the number of all nodes N in the domain (proportional to $\frac{1}{h}$), and the polynomial degree p. In particular, we have a closer look at a single RBF-FD cardinal basis function Ψ^* , of which the center node is chosen closest to the point x = 0.4. To examine the discontinuities, we measure the largest magnitude of discontinuity present in Ψ^* . The results are given in Figure 6.1, where we observe that the largest discontinuity decays as n grows. In the cases p=4and p=5 we observe that the largest discontinuity decays with the same decay rate for all tested N, except N=20 and N=100, where the discontinuity vanishes as stencil sizes become n=20 and n=100 respectively (note that n=N in these two cases, and the method is in fact global). When p=3, then the largest discontinuity vanishes (up to the round-off error level) for all involved N. Another observation is that the jump size is generally the same for each N when n is fixed. We draw two conclusions:

- For a fixed h, the discontinuities decrease as n increases.
- For a fixed n, the discontinuities remain constant as the internodal distance h is decreased.

A consequence is that the jump instability inferred from (6.19) can, to some extent, be stabilized by increasing the stencil size.

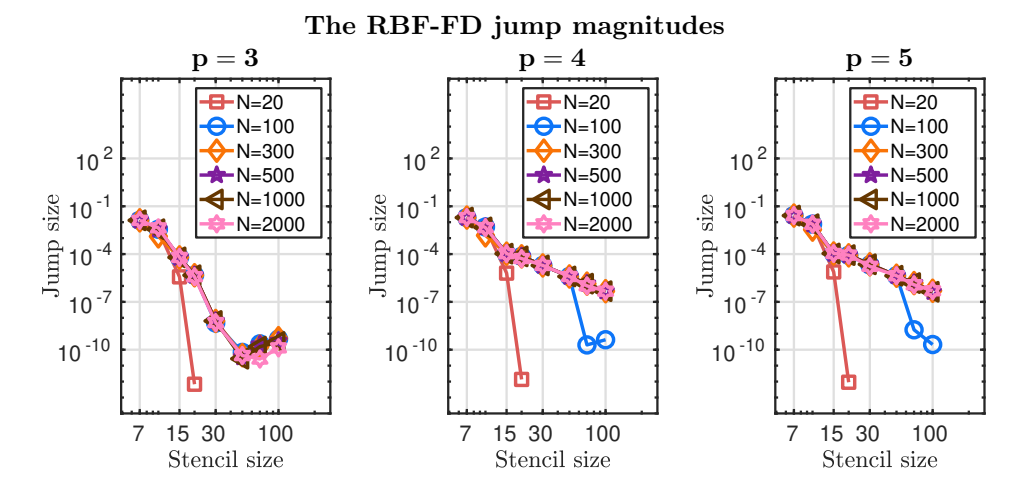


Fig. 6.1: Magnitude of the largest jump (discontinuity) in a cardinal basis function Ψ^* , as the stencil size is increased. The different curves correspond to the parameter N, the number of nodes placed on a 1D domain $\Omega_{1D} = [0, 1]$. For each stencil size and N, the observed Ψ^* is chosen such that its center node is closest to the point x = 0.4.

6.7. Definition of a penalty term for the RBF-FD method that forces the spurious jumps towards zero. A common way to stabilize the system (2.5), where the matrices are constructed using the RBF-FD method, is to supply (2.5) with a stabilization term $\gamma \mathcal{P}u_h$ on the right-hand-side of the system. Here \mathcal{P} is

normally a hyperviscosity operator and γ is scaling. In this section we provide an alternative formulation of $\mathcal P$ based on the stability estimate (6.19) where the jumps across the Voronoi edges were shown to cause a spurious growth in time. For this reason we construct $\mathcal P$ such that the jump terms $\sum_{\mathcal E_i \in \mathcal E^I} \int_{\mathcal E_i} (u_h^+ - u_h^-)^2 \, ds \to 0$. The discrete operator $\mathcal P$ and the scaling γ are given by discretizing the jump term using the oversampled matrices:

$$\mathcal{P} = (E_{+}(Y_{\mathcal{E}}, X) - E_{-}(Y_{\mathcal{E}}, X))^{T} (E_{+}(Y_{\mathcal{E}}, X) - E_{-}(Y_{\mathcal{E}}, X))$$

$$\gamma = -h_{\mathcal{E}}$$

where $Y_{\mathcal{E}}$ is the set of all midpoints on the interior Voronoi edges, see Figure 6.2. The terms $E_+(Y_{\mathcal{E}}, X)$ and $E_-(Y_{\mathcal{E}}, X)$ are unscaled global matrices of evaluation weights for evaluating the solution at $Y_{\mathcal{E}}$, constructed using the "left" stencil and the "right" stencil respectively. The $h_{\mathcal{E}} > 0$ scaling is the approximate mean distance between the points $Y_{\mathcal{E}}$, measured along the Voronoi edges.

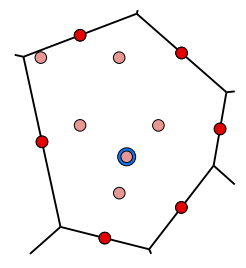


Fig. 6.2: One Voronoi cell with a set of midpoints $Y_{\mathcal{E}}$ placed over its edges (red points). The Voronoi cell has one center X point (blue point) and 6 interior evaluation Y points (pale red points).

7. Numerical experiments. In this section we provide numerical tests that (i) show a practical relation to the derived stability estimates in Section 6.2 for Kansa's method, in Section 6.3 for RBF-PUM and in Section 6.4 for the RBF-FD method, (ii) examine the convergence of the approximation error under node refinement. The domain boundary $\partial\Omega$ that we use for the experiments is in polar coordinates (r,θ) prescribed by the relation $r(\theta) = 1 - \frac{1}{3}\sin(2\theta)^2$, where $\theta \in [0, 2\pi)$. The final shape can be observed in Figure 2.1.

The initial condition that we consider is a C^6 compactly supported Wendland function $(1-r)^6 (35r^2+18r+3)$, where r is the Euclidean distance measure from the origin (0,0). The initial condition is scaled such that its support radius is of size 0.4.

Time steps for advancing the numerical solution in time and scaling the eigenvalue spectra, are computed using the relation:

(7.1)
$$\Delta t = \text{CFL} \frac{h}{\sqrt{(F_1'(t))^2 + (F_2'(t))^2}},$$

where CFL > 0 is the CFL (Courant-Friedrichs-Lax) number and F'_1 , F'_2 are the two components of the velocity field \mathbf{F}' . We consider a rotational field $\mathbf{F}'(t) = \frac{1}{2} \left[\cos(2\pi t), \sin(2\pi t) \right]$.

The approximation errors are measured as:

(7.2)
$$||e||_k = \frac{||u_h(Y, t_{\text{final}}) - u(Y, t_{\text{final}})||_k}{||u(Y, t_{\text{final}})||_k}, \quad k = \{1, 2, \infty\}.$$

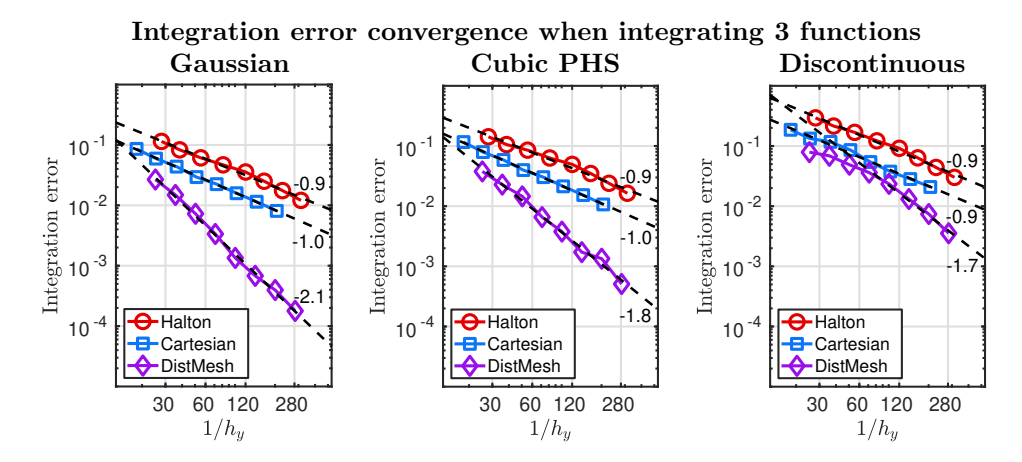


Fig. 7.1: Integration error when approximating an integral by means of oversampling, as a function of the inverse internodal distance $1/h_y$ in the evaluation point set Y. The three plots are from left to right displaying the convergence when integrating: a Gaussian function, the cubic polyharmonic (PHS) function and a discontinuous function disjointly defined by trigonometric and polynomial functions. The lines in each plot correspond to using three different evaluation point sets Y.

The point set X is obtained using the DistMesh algoritm [14] with h as input, and is then in some cases modified with a random perturbation of the magnitude 0.65 h in order to also make observations on a scattered point set. A comparison between the two instances of point sets when h = 0.09, is given in Figure 2.1. In the table below we give a relation between all considered h and the number of unknowns N.

h	0.08	0.07	0.06	0.05	0.04	0.03	0.02
1/h	12.5	14.3	16.7	20	25	33.3	50
N	400	520	713	1030	1605	2850	6420

The point set Y is in the cases when we examine the solutions to the PDE problem (1.1), obtained using the DistMesh algorithm.

7.1. Convergence of the integration error induced by oversampling. Here we numerically verify the asymptotic behavior of the integration error estimate (A.2) derived in Appendix A. We observe the convergence $\frac{|\Omega|}{M} \sum_{k=1}^{M} f(y_k) \rightarrow \int_{\Omega} f(y) d\Omega$, where $|\Omega| = \int_{\Omega} 1 d\Omega$, and the evaluation points $Y = \{y_k\}_{k=1}^{M}$ are chosen as: Halton points, Cartesian points or DistMesh points. The domain boundary that we consider is defined in the scope of Section 7, and is visualized in Figure 2.1.

Let $r_f = r_f(y_1, y_2) = (y_1^2 + y_2^2)^{1/2}$. We choose three functions that we integrate: a Gaussian function $f_1(y_1, y_2) = e^{-3r_f}$ (infinitely smooth), a cubic polyhanormic spline $f_2(y_1, y_2) = r_f^3$ (twice continuously differentiable), a discontinuous function defined by $f_3(y_1, y_2) = 0.2 + \sin(4\pi y_1 y_2)$ when $r_f \leq 0.5$, $f_3(y_1, y_2) = y_1^3 y_2$ when $0.5 < r_f \leq 0.7$ and $f_3(y_1, y_2) = 0.4 + \cos(4\pi y_1 y_2)$ when $r_f > 0.7$.

The result is given in Figure 7.1, where we observe that the convergence trend is 1 for all considered integrands, when using Halton and Cartesian point sets for evaluating the integrals. We also observe that the Cartesian point set in the considered case gives a smaller integration error. The convergence trend when the DistMesh

Kansa's method: eigenvalue spectra, DistMesh nodes

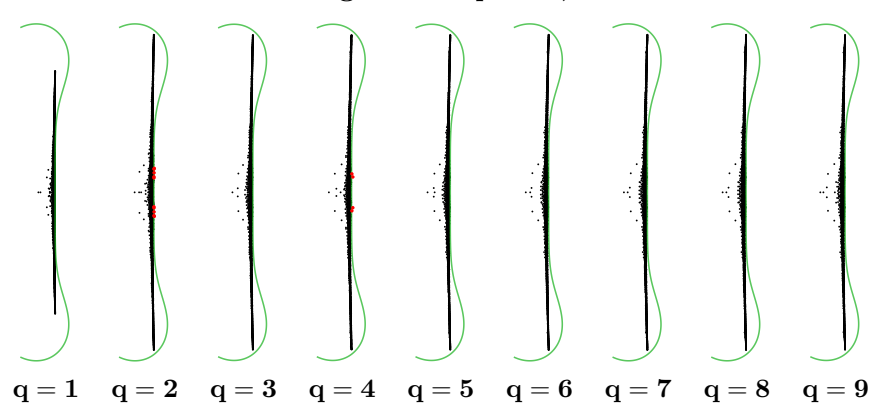


Fig. 7.2: Eigenvalue spectra (black dots) of the advection operator with 0 inflow boundary conditions, when Kansa's method is used, as the oversampling parameter q is increased (left to right). The green line is the boundary of the classical explicit Runge-Kutta 4 stability region. The red dots are the eigenvalues that are not contained inside the stability region.

point set is used tends towards 2. The most significant difference between the point sets is that the internodal distance near the domain boundary is following a smooth distribution in the DistMesh point set case, and we speculate that this is the reason for observing a larger convergence trend. In any case, the integration error due to the oversampling decays asymptotically with at least an order 1 in 2D, as derived in (A.2).

We note that we observed very similar convergence trends of the integration error when integrating the three considered functions over a different choice of domain boundary, in polar coordinates given by $r(\theta) = 1 + 1/10(\sin(7t) + \sin(t))$, $\theta \in [0, 2\pi]$. A visualization of that domain boundary is available in [25, Fig. 3].

7.2. Eigenvalue spectra for Kansa's RBF method, RBF-PUM and the RBF-FD method. In Section 6.5 we showed a relation between the semi-discrete stability estimate and the eigenvalues of the ODE system matrix $(E_h^T E_h)^{-1} (E_h^T D_h)$ from (2.7). When computing the eigenvalue spectra we impose a 0 inflow boundary condition by eliminating the corresponding columns and rows of $(E_h^T E_h)^{-1} (E_h^T D_h)$. For fixed parameters h and p we test how an increase in the oversampling parameter q influences the stability through the eigenvalue spectra. Note that as $h_y \to 0$, then $q \to \infty$, and the integration error in the stability estimate (6.10) goes to 0. Note also that when q = 1, we have that $h_y = h$, which is the limit case of the oversampling that yields the collocated discretization.

The result for Kansa's method with the DistMesh X points when h=0.03 and p=4, is drawn in Figure 7.2. We observe that the spectra are alternating between being stable and having spurious eigenvalues, until q=4, and then become stable for $q \geq 5$. A similar result is also observed when the X points are randomly perturbed in Figure 7.3. Both results are aligned with the stability result from Section 6.2: for an oversampling that is large enough, Kansa's method is stable when discretizing the linear advection problem.

Kansa's method: eigenvalue spectra, perturbed DistMesh nodes

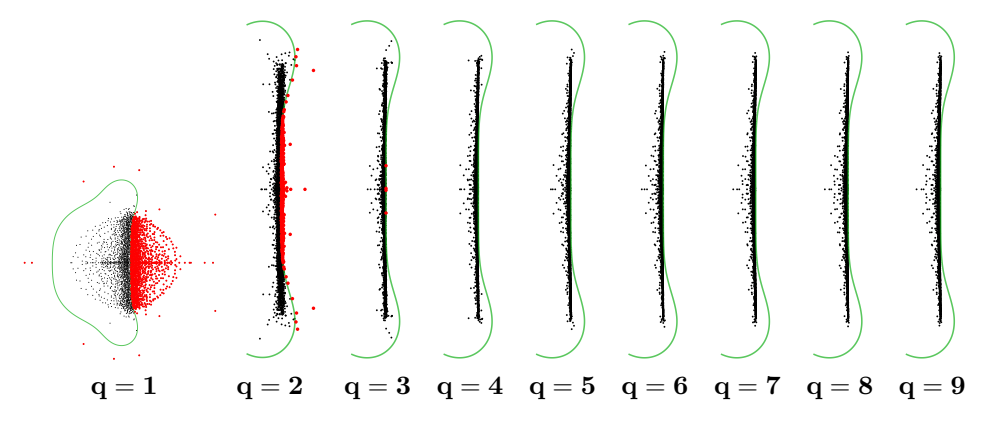


Fig. 7.3: Eigenvalue spectra (black dots) of the advection operator with 0 inflow boundary conditions, when Kansa's method is used on randomly perturbed DistMesh X points (h = 0.03), as the oversampling parameter q is gradually increased. The green line is the full stability region (q = 1) or its boundary (q > 1), of the classical explicit Runge-Kutta 4 method. The red dots are the eigenvalues that are not contained inside the stability region.

The result for RBF-PUM when h = 0.03 and p = 4 is given in Figure 7.4. Here we only consider the randomly perturbed DistMesh point set X. We observe that the eigenvalue spectra are stable when $q \ge 5$, but otherwise unstable. This is aligned with the stability result from Section 6.3.

The results for the unstabilized RBF-FD method with h = 0.03 are given in Figure 7.5. Here we use an unperturbed DistMesh point set X. We test the eigenvalue spectra as the stencil size n varies and the monomial basis degree p=2 is fixed. When n=12(obtained from $n=2\binom{p+2}{2}$), the eigenvalue spectra contain spurious eigenvalues for each choice of the oversampling parameter, even when the oversampling is unusually large. This is in agreement with the semi-discrete stability estimate (6.19). The jump term in the estimate has a non-negligible size and an arbitrary sign. If the accumulation of the jump terms results in a large positive number, then we are, according to the discussion in Section 6.5, expected to observe spurious eigenvalues. From the same figure we further observe that when we keep p=2, but increase the stencil size to n=30, the eigenvalue spectra become stable for $q\geq 3$. This is again in agreement with the estimate (6.19), when the estimate is augmented with the result from Figure (6.1) which states that the magnitude of the jumps vanishes as nis increased. Thus, large stencil sizes improve the stability properties of the RBF-FD method. We make a remark that the eigenvalue spectra were stable for larger p and n computed according to $n=2\binom{p+2}{2}$. This makes sense, since larger p are associated with larger n, and thus smaller jumps. However, we can not say in general that the RBF-FD method is stable for large p, since the size of the jumps will inevitably depend on the choice of the point set X.

The results for the jump-stabilized RBF-FD method are collected in Figure 7.6. We again use p=2 and two different stencil sizes, n=12 and n=30, but now we add the jump penalty term defined in Section 6.7 that forces the spurious jumps in the RBF-FD cardinal basis functions towards 0. We also use the randomly perturbed

RBF-PUM: eigenvalue spectra, perturbed DistMesh nodes

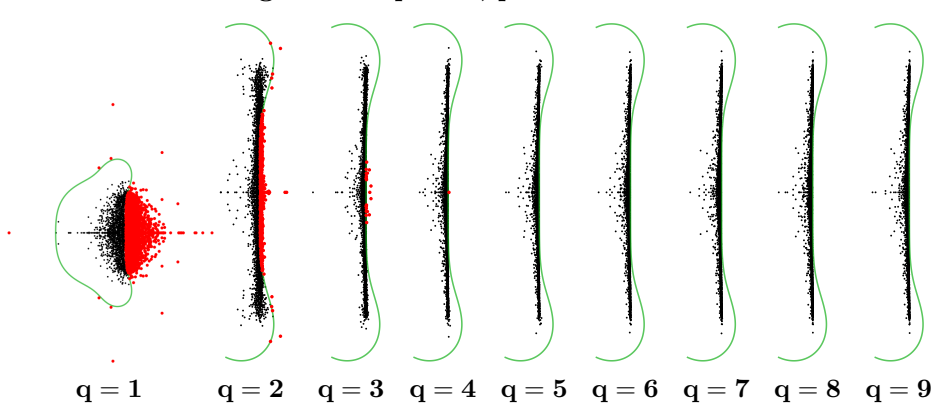
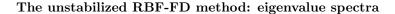


Fig. 7.4: Eigenvalue spectra (black dots) of the advection operator with 0 inflow boundary conditions, when RBF-PUM is used on randomly perturbed DistMesh X points (h=0.03), as the oversampling parameter q is gradually increased. The green line is the full stability region (q=1) or its boundary (q>1), of the classical explicit Runge-Kutta 4 method. The red dots are the eigenvalues that are not contained inside the stability region.

DistMesh point set in order to not give the stabilization term a favorable starting point. From the figure we observe that the eigenvalue spectrum around the imaginary axis is now stable also in the n=12 case, as opposed to the unstabilized method in Figure 7.5. We note that we also observed stable eigenvalue spectra for higher choices of p when the jump stabilization term was used and we chose n according to the standard formula $n=2\binom{p+2}{2}$. Another remark is that the CFL numbers have to be chosen smaller when the jumps are large (small p and consequently small n), compared with the case when the RBF-FD method is not stabilized using the jump penalty term. Thus, an effective strategy to stabilize the RBF-FD method is to always add the jump penalty term and possibly, at the same time, increase the stencil size when p is small (p=1,2).

7.3. Convergence of the approximation error under node refinement for RBF-PUM and the RBF-FD method. We examine the convergence of the approximation error as a function of h, for different choices of p and a fixed q. The final time of the simulation is set to $t_{\text{final}} = 3$. The time step is computed according to CFL = 0.2, which is intentionally kept low, so that the resulting time steps are small and that the spatial approximation errors dominate.

The results for RBF-PUM, the unstabilized RBF-FD method and the jump-stabilized RBF-FD method, using q=9, are shown in Figure 7.7. We observe that all the methods converge for all p with a rate at least p-1. In the unstabilized RBF-FD case, the eigenvalue spectra for p=2 were shown to be unstable in Figure 7.5, however, the approximation error was still convergent. This is because the spurious eigenvalues have not triggered a visible instability until $t_{\rm final}=3$. A longer simulation that shows an instability is performed in the section that follows. The approximation error in the jump-stabilized RBF-FD case is at least as small as in the unstabilized RBF-FD case. We conclude that the proposed jump-stabilization is effective for the



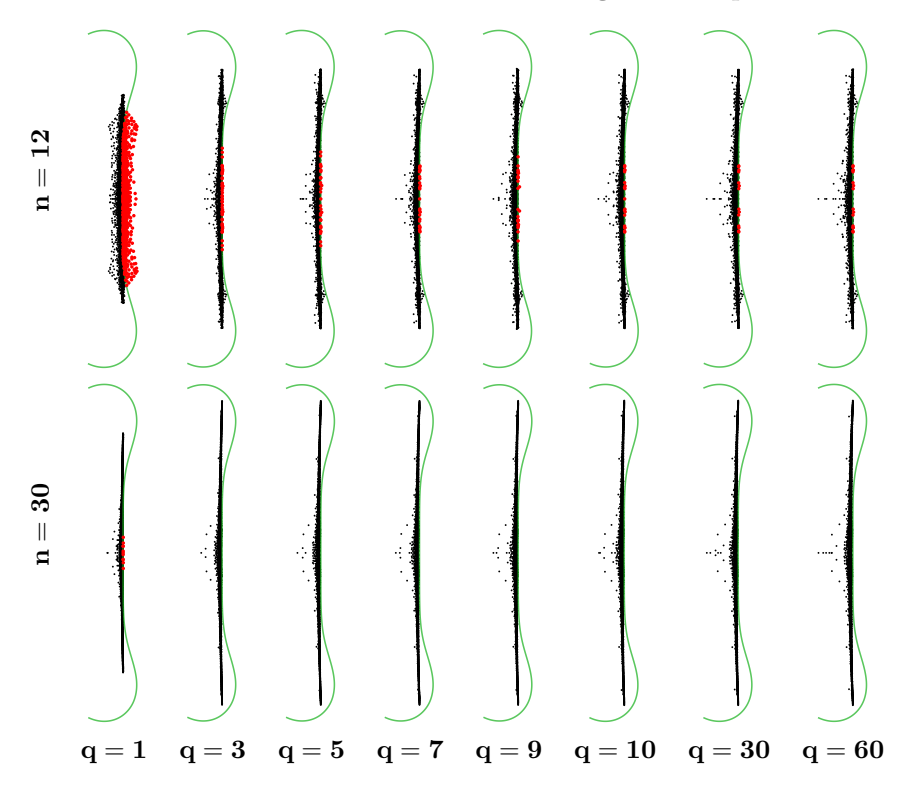


Fig. 7.5: Eigenvalue spectra (black dots) of the advection operator with 0 inflow boundary conditions, when the RBF-FD method is used on DistMesh X points (h=0.03), as the oversampling parameter q (columns) is gradually increased. The monomial basis degree is fixed to p=2. The two rows correspond to a different stencil size n. The green line is the boundary of the stability region for the classical explicit Runge-Kutta 4 method. The red dots are the eigenvalues that are not contained inside the stability region.

considered simulation case.

Similar convergence rates were also observed in 1-norm and ∞ -norm, for all considered methods.

7.4. Energy of the numerical solution as a function of time for Kansa's RBF method, RBF-PUM and the RBF-FD method. Here we examine the energy of the numerical solution with respect to time, for all three methods. The purpose is to examine the stability of the methods, but also to observe whether the energy is conserved. We measure the energy of the numerical solution relative to the energy of the initial condition as $\|u_h(Y,t)\|_{\ell_2}^2/\|u_h(Y,0)\|_{\ell_2}^2$, where the norm is defined in (6.2). The final time of the simulation is set to $t_{\text{final}} = 20$, which makes the compactly supported initial condition rotate around the origin 20 times, without interacting with the boundary of the domain, so that the energy of the solution is (ideally) not changing with time. The CFL number is set to CFL = 0.6. We test the conservation for different choices of h, p and q.

Jump-stabilized RBF-FD method: eigenvalue spectra

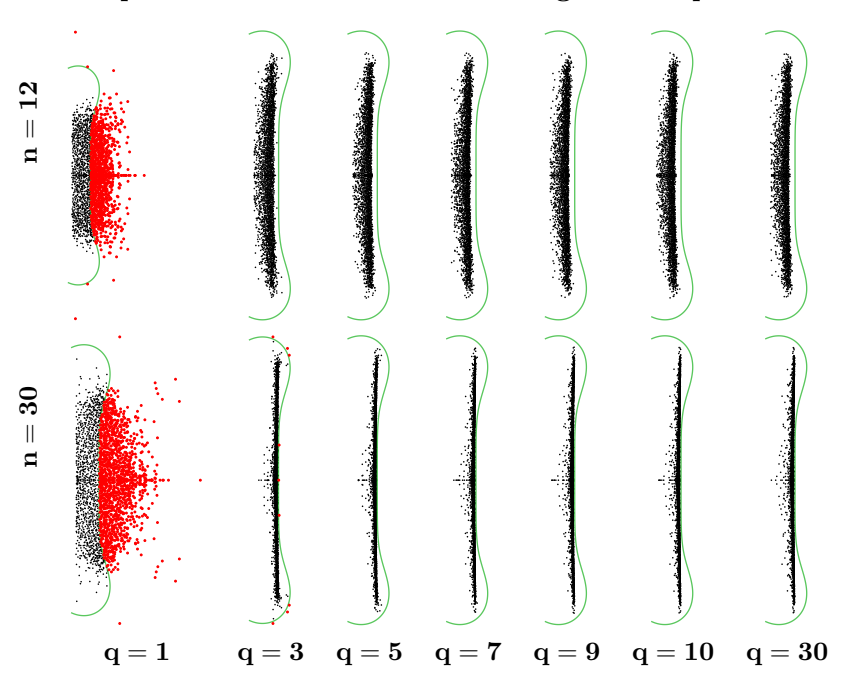


Fig. 7.6: Eigenvalue spectra (black dots) of the advection operator with 0 inflow boundary conditions, when the RBF-FD method is stabilized using the jump penalty term and used in combination with randomly perturbed DistMesh X points (h=0.03), as the oversampling parameter q (columns) is gradually increased. The monomial basis degree is fixed to p=2. The two rows correspond to a different stencil size n. The green line is the boundary of the stability region for the classical explicit Runge-Kutta 4 method. The red dots are the eigenvalues that are not contained inside the stability region.

The result for Kansa's RBF method is displayed in Figure 7.8, where we fixed p=5. Firstly, we observe that the method is stable for all considered parameters, as the energy is either constant or decaying. This is in agreement with the semi-discrete stability estimate (6.10). Secondly, the energy decays when h is large, and then gets asymptotically more constant as h is decreased. Thirdly, the oversampling does not significantly improve the conservation of energy. Results for RBF-PUM are collected in Figure 7.9. The results are very similar to the Kansa's method case, except that the method is unstable for some h and p when the oversampling is too small (q=6). The method does get stable when the oversampling is larger (q=9, q=12), which is in agreement with the stability estimate derived in Section 6.3. We also observe that RBF-PUM is slightly more diffusive when p=2 and p=12 and p=12 is small, compared with Kansa's RBF method.

The unstabilized RBF-FD method is examined through Figure 7.10. Here we observe that the method is unstable for all h and q when p=2. This is in agreement with the stability estimate (6.19), but also with the examination of the stability of the eigenvalue spectra in Figure 7.5. Further, when p=2 we observe that the method

Convergence under node refinement in 2-norm **RBF-PUM** RBF-FD RBF-FD, stabilized 10 10 10 10⁻² 10⁻² 10 10⁻³ e10 10 10 -4 10 ⁻⁴ 10 10⁻⁵ 10 10 -p=4 **1**−p=5 10 10 10 20 40 80 10 20 40 80 20 40 10 10 80 1/h1/h

Fig. 7.7: Convergence of the approximation error in the relative 2-norm, as a function of the inverse internodal distance 1/h, for three methods: RBF-PUM, unstabilized RBF-FD and jump-stabilized RBF-FD. Different lines in the plots correspond to different choices of the monomial basis degree p used to construct the stencil-based approximations. The oversampling parameter is fixed to q=9. The time step to advance the solution in time is computed using CFL = 0.2.

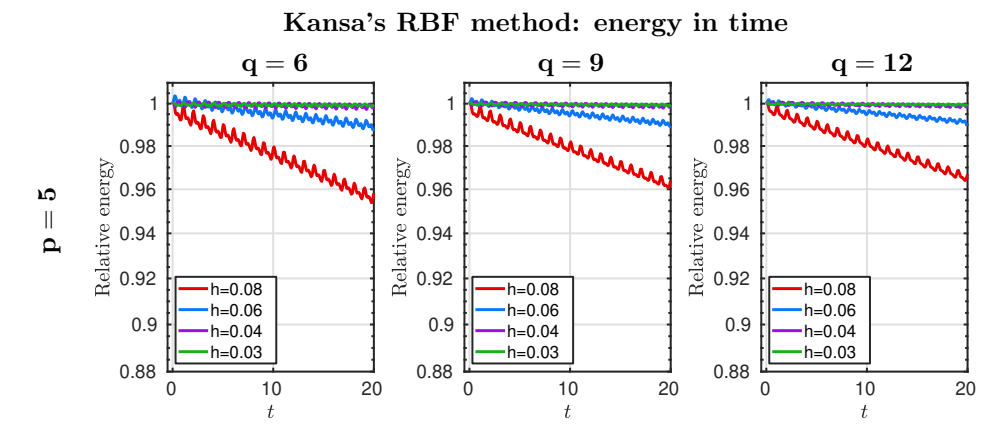


Fig. 7.8: Energy as a function of time, relative to the energy of the initial condition (Kansa's RBF method), measured in the ℓ_2 norm, for different choices of: the internodal distance h (different lines in figures), the oversampling parameter q (columns) and the monomial basis degree p=5, used to construct the global approximation. CFL = 0.6 was used to determine the time step.

does not blow up until t=3, at which point we made the results in Figure 7.7. When p=5 the method is stable for all choices of the considered parameters, which is due to an increase in n (compared with the case p=2) and smaller jumps as a consequence, as already pointed out in Section 7.2 through Figure 7.5. We emphasize that we can not guarantee the unstabilized RBF-FD method to be stable when p is large, as

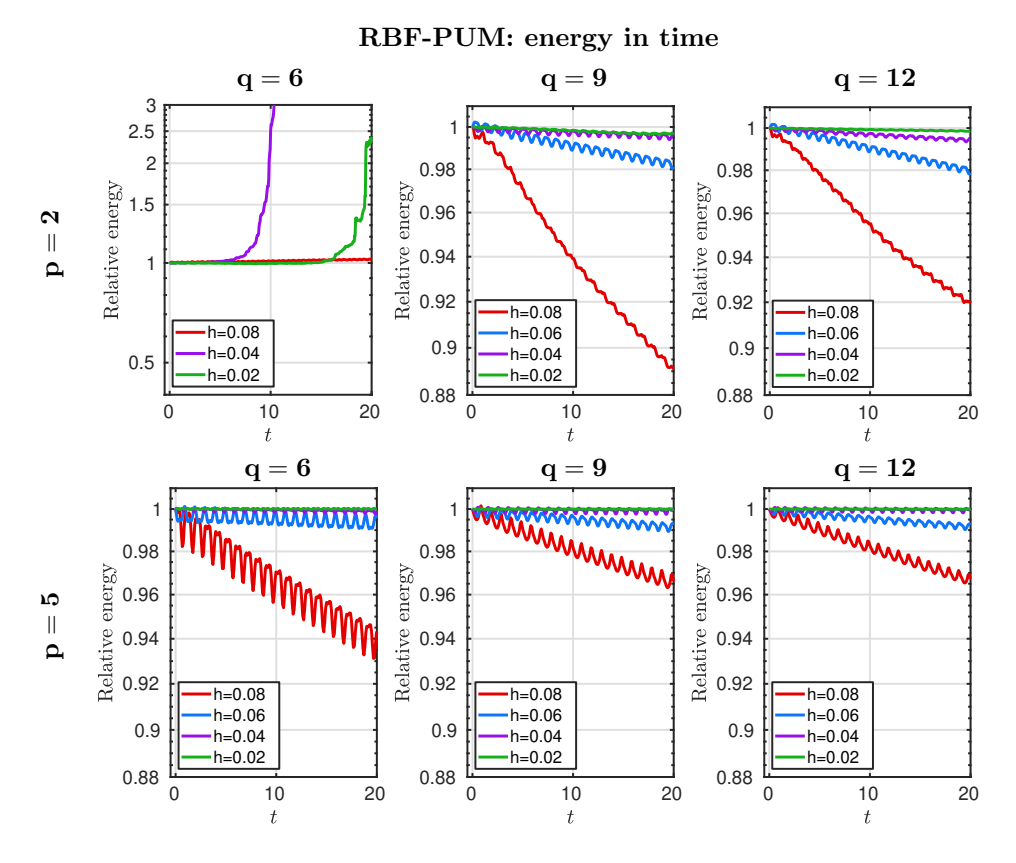


Fig. 7.9: Energy as a function of time, relative to the energy of the initial condition (RBF-PUM), measured in the ℓ_2 norm, for different choices of: the internodal distance h (different lines in figures), the oversampling parameter q (columns) and the monomial basis degrees p (rows) which are used to construct the patch-based approximation. CFL = 0.6 was used to determine the time step.

the choice of n at which the jumps become small enough can depend on many other parameters.

The results for the jump-stabilized RBF-FD method are given in Figure 7.11. For all p, q and h, the method is stable in time. When p=2, the method is diffusive for a large h. When p=5, the method is less diffusive for a large h. We observe that as h is decreased, the conservation of energy is being asymptotically established.

7.5. Maximal CFL numbers for Kansa's RBF method, RBF-PUM and the RBF-FD method. For all three methods, we examined the maximal CFL numbers that still allow stable time stepping when using the explicit classical Runge-Kutta 4 method to advance the solution in time. We are in particular interested in how the oversampling influences the CFL numbers and whether the jump-stabilization for the RBF-FD method has a negative effect on the maximal time step. The relation between Δt and CFL is given in (7.1). We fix the mean internodal distance in the perturbed DistMesh point set X to h = 0.04 and compute the maximal CFL numbers as a function of the oversampling parameters q = 5, 6, ..., 14 and the monomial basis

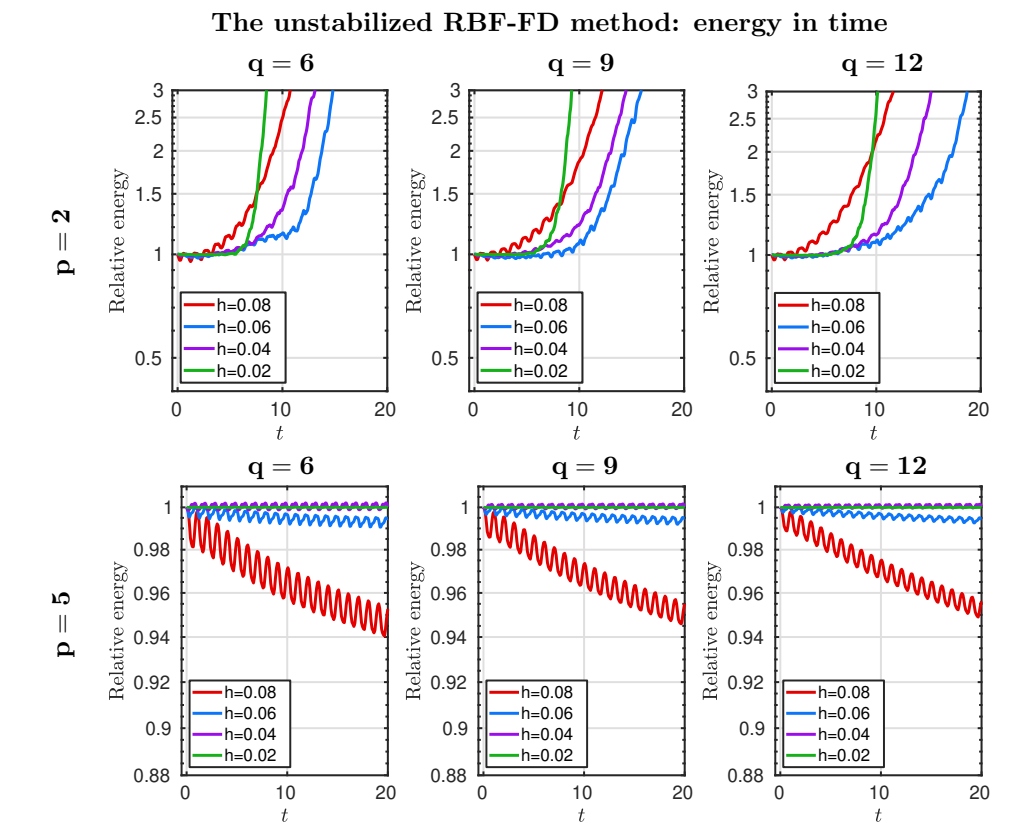


Fig. 7.10: Energy as a function of time, relative to the energy of the initial condition (unstabilized RBF-FD), measured in the ℓ_2 norm, for different choices of: the internodal distance h (different lines in figures), the oversampling parameter q (columns) and the monomial basis degrees p (rows) which are used to construct the stencil-based approximation. CFL = 0.6 was used to determine the time step.

degrees p=2,3,4,5,6. It turns out that for all the methods the CFL number has to be taken smaller as the oversampling parameter increases, however, the decay in the CFL number is small. The most significant difference between the smallest and the largest CFL numbers per a fixed p is only 0.07%, measured relatively to the largest CFL number per a fixed p. Thus, an increase in the oversampling does not catastrophically impact the size of Δt .

8. Final remarks. In this paper we investigated the stability properties of Kansa's RBF method, RBF-PUM and the RBF-FD method, when applied to a time-dependent hyperbolic problem. Our analysis was made for a linear advection problem with a divergence free velocity field.

We derived that the ℓ_2 -stability in time for Kansa's RBF method and RBF-PUM, is for a fixed h, controllable by h_y which is inversely proportional to the oversampling parameter q. When collocation is used instead of oversampling, then q = 1, and the stability control through q is lost. The ℓ_2 -stability in time of the RBF-FD method also depends on q (controllable), but also on the jump terms across the interfaces

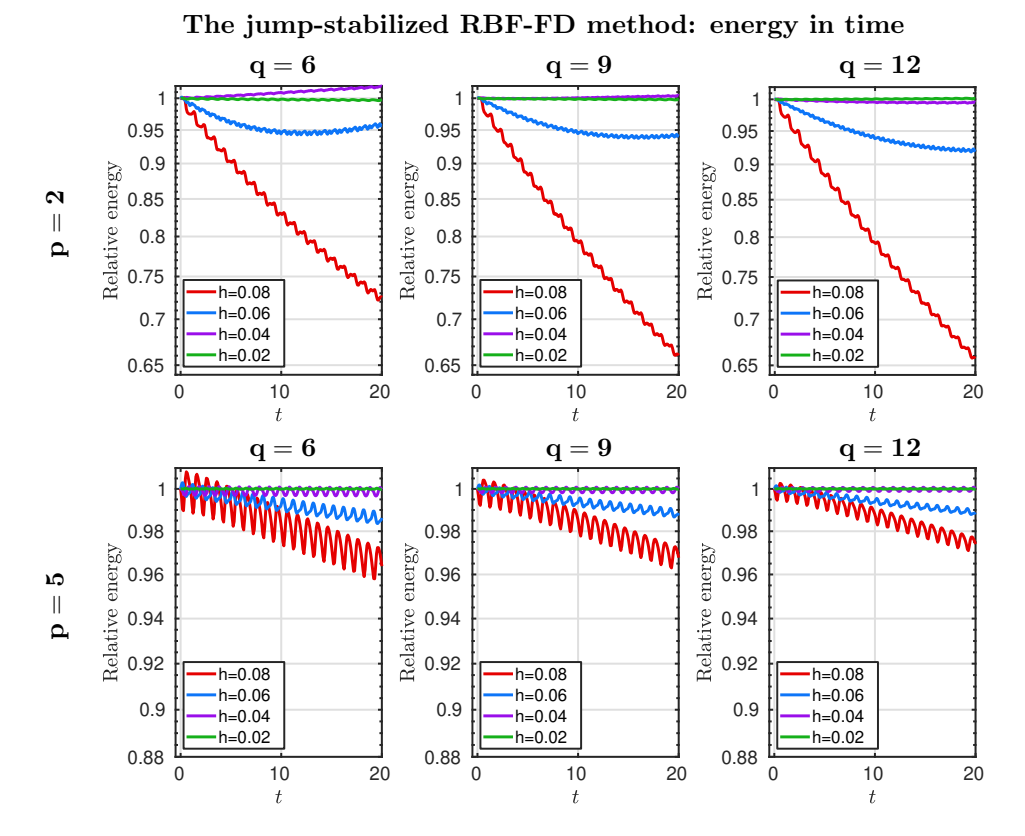


Fig. 7.11: Energy as a function of time, relative to the energy of the initial condition (jump-stabilized RBF-FD), measured in the ℓ_2 norm, for different choices of: the internodal distance h (different lines in figures), the oversampling parameter q (columns) and the monomial basis degrees p (rows) which are used to construct the stencil-based approximation. CFL = 0.6 was used to determine the time step.

of the Voronoi cells centered at each $x_i \in X$. As we demonstrated numerically, a possibility to control the size of the jumps is to increase the stencil size n, however, this is a computationally expensive approach since an increase to n gives an increase in the density of the discretization matrices. We provided a special penalty term that controls the jump term for any n, and in this way stabilizes the method.

Numerical experiments confirmed that by increasing the oversampling, the stability of Kansa's RBF method and RBF-PUM was being manifested, since we could find a CFL number such that the eigenvalue spectra were fully contained in the classical explicit Runge-Kutta 4 stability region. The experiments also confirmed that the RBF-FD method can not be stabilized only by increasing the oversampling, unless we also decrease the spurious jump term at the same time.

Overall, we established a theoretical framework and illustrated some of the practical implications, which can, in the future, be used for further improvements of the three considered RBF methods.

Appendix A. The integration error induced by the oversampling, for piecewise continuous functions. In this section we derive an estimate for the

integration error $\frac{|\Omega|}{M}\sum_{i=1}^M f(y_i) - \int_\Omega f \,d\Omega$, where $y_i \in \Omega \subset \mathbb{R}^2$ and $|\Omega| = \int_\Omega 1 \,d\Omega$. The finite-dimensional piecewise smooth integrand $f \in L_2(\Omega)$. At the same time we also have that $f \in C^k(K_i)$, k > 0, i = 1, ..., N, where $\cup_{i=1}^N K_i = \Omega$ is the set of Voronoi regions generated by point set X, subjected to the closure of Ω . In the estimate, we use regions that intersect the domain boundary. Therefore we introduce the modified integrand $\bar{f} = fg$, where g = 1 on Ω and g = 0 elsewhere. We limit the derivation to the case where the point set Y of size M has a Cartesian layout with grid size and internodal distance h_y , subjected to the domain Ω . We let $y_{\Gamma(i,j)} \in Y$, $j = 1, ..., q_i$ be the points that sample the Voronoi region K_i , where Γ is an operator relating the local index of an evaluation point contained in K_i , to a global index in Y. For a quasi uniform node set X, $q_i = \alpha_i q$ with $\alpha_i \approx 1$. We bound the integration error using boxes B_{ij} with side h_y , centered at $y_{\Gamma(i,j)}$. Out of the q_i boxes there are n_i boxes such that $B_{ij} \subset K_i$, while $q_i - n_i$ extend outside K_i . Due to the area to boundary relation, the box numbers can be bounded by $n_i \leq c_A q$ and $(q_i - n_i) \leq c_B \sqrt{q}$. Furthermore, we need to add some auxiliary boxes \tilde{B}_{ij} that do not have a corresponding center point in Y, but are needed to cover all of Ω . In the same way, the number n_Ω of these boxes can be bounded by $n_\Omega \leq c_\Omega \sqrt{N} \sqrt{q}$, since the number of interior boxes B_{ij} is M = Nq.

The numerical integration over one box is written as $I_h(B_{ij}) = \frac{|\Omega|}{M} \bar{f}(y_{\Gamma(i,j)}) = |B_{ij}| \bar{f}(y_{\Gamma(i,j)}) = \int_{B_{ij}} \bar{f}(y_{\Gamma(i,j)}) \, dy$. Furthermore, we note that due to the continuity of f on K_i , the mean value theorem leads to $\bar{f}(y) = \bar{f}(y_{\Gamma_{ij}}) + (y - y_{\Gamma_{ij}}) \cdot \nabla \bar{f}(\xi)$, where $\xi = \theta y + (1 - \theta) y_{\Gamma_{ij}}, \ 0 \le \theta \le 1, \ y \in K_i$. The integration error over B_{ij} then becomes:

$$I(B_{ij}) - I_h(B_{ij}) = \int_{B_{ij}} \bar{f}(y) - \bar{f}(y_{\Gamma_{ij}}) \, dy = \int_{B_{ij} \cap K_i} (y - y_{\Gamma_{ij}}) \cdot \nabla \bar{f}(\xi(y)) \, dy + \int_{B_{ij} \setminus (B_{ij} \cap K_i)} \bar{f}(y) - \bar{f}(y_{\Gamma_{ij}}) \, dy.$$

The integration error over the whole domain can be estimated as:

$$\begin{split} |I(\Omega) - I_{h}(\Omega)| &= \left| \sum_{i=1}^{n_{\Omega}} \int_{\tilde{B}_{ij}} \bar{f}(y) \, dy + \sum_{i=1}^{N} \sum_{j=1}^{q_{i}} I(B_{ij}) - I_{h}(B_{ij}) \right| \\ &\leq \sum_{i=1}^{n_{\Omega}} \left| \int_{\tilde{B}_{ij}} \bar{f}(y) \, dy \right| + \sum_{i=1}^{N} \sum_{j=1}^{q_{i}} \left| \int_{B_{ij} \cap K_{i}} (y - y_{\Gamma_{ij}}) \cdot \nabla \bar{f}(\xi(y)) \, dy \right| \\ &+ \sum_{i=1}^{N} \sum_{j=1}^{q_{i} - n_{i}} \left| \int_{B_{ij} \setminus (B_{ij} \cap K_{i})} \bar{f}(y) - \bar{f}(y_{\Gamma_{ij}}) \, dy \right| \\ &\leq c_{\Omega} \sqrt{N} \sqrt{q} \max_{ij} |\tilde{B}_{ij}| \max_{ij} ||f||_{L_{\infty}(K_{ij})} + \\ &+ Nq \max_{i} \alpha_{i} \max_{ij} |B_{ij} \cap K_{i}| \frac{h_{y}}{\sqrt{2}} \max_{ij} ||\nabla f||_{L_{\infty}(K_{ij})} \\ &+ c_{B} N \sqrt{q} \max_{ij} |B_{ij} \setminus (B_{ij} \cap K_{i})| 2 \max_{ij} ||f||_{L_{\infty}(K_{ij})} + \\ &\leq (\sqrt{|\Omega|} c_{\Omega} + 2|\Omega| c_{B} h^{-1}) h_{y} \max_{ij} ||f||_{L_{\infty}(K_{ij})} + \\ &+ |\Omega| \frac{\max_{i} \alpha_{i}}{\sqrt{2}} h_{y} \max_{ij} ||\nabla f||_{L_{\infty}(K_{ij})}, \end{split}$$

where we in the last step used $|B_{ij}| = h_y^2$, $|B_{ij} \cap K_i| \leq |B_{ij}|$, $|B_{ij} \setminus (B_{ij} \cap K_i)| \leq$

 $|B_{ij}|, \sqrt{N}\sqrt{q} = \sqrt{|\Omega|} h_y^{-1}$, and $1/\sqrt{q} = \frac{h_y}{h}$. We finish the estimate by using an inverse inequality $\max_{ij} \|\nabla f\|_{L_{\infty}(K_{ij})} \le C_I h^{-1} \max_{ij} \|f\|_{L_{\infty}(K_{ij})}$ from [5], where C_I is independent of h, to arrive to: (A.2)

$$|I(\Omega) - I_h(\Omega)| \le (\sqrt{|\Omega|}c_{\Omega} + 2|\Omega|c_B h^{-1} + |\Omega| \frac{\max_i \alpha_i}{\sqrt{2}} C_I h^{-1}) h_y \max_{ij} ||f||_{L_{\infty}(K_{ij})}$$

$$\le C_{\int} h^{-1} h_y \max_{ij} ||f||_{L_{\infty}(K_{ij})},$$

where $C_{\int} = \sqrt{|\Omega|}c_{\Omega} + |\Omega|(2c_B + \frac{\max_i \alpha_i}{\sqrt{2}}C_I)$. We observe that for a fixed h, the integration error induced by oversampling asymptotically approaches 0 as $h_y \to 0$.

Acknowledgments. We thank Víctor Bayona from Universidad Carlos III de Madrid and Katharina Kormann from Uppsala University for fruitful discussions.

REFERENCES

- [1] K. Aiton, A radial basis function partition of unity method for transport on the sphere, master's thesis, 2014.
- [2] G. A. BARNETT, A Robust RBF-FD Formulation based on Polyharmonic Splines and Polynomials, Ph.D. thesis, University of Colorado at Boulder, Dept. of Applied Mathematics, Boulder, CO, USA, 2015.
- [3] V. BAYONA, An insight into RBF-FD approximations augmented with polynomials, Comput. Math. Appl., 77 (2019), pp. 2337–2353, https://doi.org//10.1016/j.camwa.2018.12.029.
- [4] V. BAYONA, N. FLYER, B. FORNBERG, AND G. A. BARNETT, On the role of polynomials in RBF-FD approximations: II. Numerical solution of elliptic PDEs, J. Comput. Phys., 332 (2017), pp. 257–273, https://doi.org/10.1016/j.jcp.2016.12.008.
- [5] S. C. Brenner and L. R. Scott, The mathematical theory of finite element methods, vol. 15 of Texts in Applied Mathematics, Springer, New York, third ed., 2008, https://doi.org/10.1007/978-0-387-75934-0, https://doi.org/10.1007/978-0-387-75934-0.
- [6] M. CHEN, K. C. CHEUNG, AND L. LING, A kernel-based least-squares collocation method for surface diffusion, 2021, https://arxiv.org/abs/2109.03409.
- [7] B. FORNBERG AND N. FLYER, A primer on radial basis functions with applications to the geosciences, vol. 87 of CBMS-NSF Regional Conference Series in Applied Mathematics, Society for Industrial and Applied Mathematics (SIAM), Philadelphia, PA, 2015, https://doi.org/10.1137/1.9781611974041.ch1, https://doi.org/10.1137/1.9781611974041.ch1.
- [8] B. FORNBERG AND E. LEHTO, Stabilization of RBF-generated finite difference methods for convective PDEs, J. Comput. Phys., 230 (2011), pp. 2270–2285, https://doi.org/10.1016/ j.jcp.2010.12.014, https://doi.org/10.1016/j.jcp.2010.12.014.
- [9] J. GLAUBITZ AND A. GELB, Stabilizing radial basis function methods for conservation laws using weakly enforced boundary conditions, J. Sci. Comput., 87 (2021), pp. Paper No. 40, 29, https://doi.org/10.1007/s10915-021-01453-8, https://doi.org/10.1007/ s10915-021-01453-8.
- [10] J. GLAUBITZ, E. LE MELEDO, AND P. ÖFFNER, Towards stable radial basis function methods for linear advection problems, Comput. Math. Appl., 85 (2021), pp. 84–97, https://doi. org/10.1016/j.camwa.2021.01.012, https://doi.org/10.1016/j.camwa.2021.01.012.
- [11] E. J. Kansa, Multiquadrics—a scattered data approximation scheme with applications to computational fluid-dynamics. II. Solutions to parabolic, hyperbolic and elliptic partial differential equations, Comput. Math. Appl., 19 (1990), pp. 147–161, https://doi.org/10.1016/0898-1221(90)90271-K, https://doi.org/10.1016/0898-1221(90)90271-K.
- [12] J. M. MARTEL AND R. B. PLATTE, Stability of radial basis function methods for convection problems on the circle and sphere, J. Sci. Comput., 69 (2016), pp. 487–505, https://doi. org/10.1007/s10915-016-0206-9, https://doi.org/10.1007/s10915-016-0206-9.
- [13] M. NAZAROV, Convergence of a residual based artificial viscosity finite element method, Comput. Math. Appl., 65 (2013), pp. 616–626, https://doi.org/10.1016/j.camwa.2012.11.003, https://doi.org/10.1016/j.camwa.2012.11.003.
- [14] P.-O. Persson and G. Strang, A simple mesh generator in Matlab, SIAM Rev., 46 (2004), pp. 329–345, https://doi.org/10.1137/S0036144503429121, https://doi.org/10. 1137/S0036144503429121.

- [15] V. SHANKAR, The overlapped radial basis function-finite difference (RBF-FD) method: a generalization of RBF-FD, J. Comput. Phys., 342 (2017), pp. 211–228, https://doi.org/10.1016/j.jcp.2017.04.037, https://doi.org/10.1016/j.jcp.2017.04.037.
- [16] V. SHANKAR AND A. L. FOGELSON, Hyperviscosity-based stabilization for radial basis function-finite difference (RBF-FD) discretizations of advection-diffusion equations, J. Comput. Phys., 372 (2018), pp. 616–639, https://doi.org/10.1016/j.jcp.2018.06.036, https://doi.org/10.1016/j.jcp.2018.06.036.
- [17] V. SHANKAR AND G. B. WRIGHT, Mesh-free semi-Lagrangian methods for transport on a sphere using radial basis functions, J. Comput. Phys., 366 (2018), pp. 170–190, https://doi.org/ 10.1016/j.jcp.2018.04.007, https://doi.org/10.1016/j.jcp.2018.04.007.
- [18] V. SHANKAR, G. B. WRIGHT, AND A. L. FOGELSON, An efficient high-order meshless method for advection-diffusion equations on time-varying irregular domains, Journal of Computational Physics, (2021), p. 110633, https://doi.org/https://doi.org/10.1016/j.jcp.2021. 110633, https://www.sciencedirect.com/science/article/pii/S0021999121005283.
- [19] V. SHANKAR, G. B. WRIGHT, AND A. NARAYAN, A robust hyperviscosity formulation for stable RBF-FD discretizations of advection-diffusion-reaction equations on manifolds, SIAM J. Sci. Comput., 42 (2020), pp. A2371–A2401, https://doi.org/10.1137/19M1288747, https://doi.org/10.1137/19M1288747.
- [20] D. SHEPARD, A two-dimensional interpolation function for irregularly-spaced data, in Proceedings of the 1968 23rd ACM National Conference, ACM '68, New York, NY, USA, 1968, Association for Computing Machinery, p. 517–524, https://doi.org/10.1145/800186.810616, https://doi.org/10.1145/800186.810616.
- [21] A. I. TOLSTYKH, On using RBF-based differencing formulas for unstructured and mixed structured-unstructured grid calculations, in Proceedings of the 16th IMACS World Congress on Scientific Computation, Applied Mathematics and Simulation, Lausanne, Switzerland, 2002.
- [22] I. TOMINEC, Parallel localized radial basis function methods for the shallow water equations on the sphere, master's thesis, Mar 2017. pruefer: Bungartz, Hans-Joachim.
- [23] I. TOMINEC, Rectangular and square RBF-FD matrices in MATLAB. https://github.com/ IgorTo/rbf-fd, 2021, https://doi.org/10.5281/zenodo.4525550.
- [24] I. Tominec and E. Breznik, An unfitted RBF-FD method in a least-squares setting for elliptic PDEs on complex geometries, J. Comput. Phys., 436 (2021), pp. 110283, 24, https://doi.org/10.1016/j.jcp.2021.110283, https://doi.org/10.1016/j.jcp.2021.110283.
- [25] I. TOMINEC, E. LARSSON, AND A. HERYUDONO, A least squares radial basis function finite difference method with improved stability properties, SIAM J. Sci. Comput., 43 (2021), pp. A1441-A1471, https://doi.org/10.1137/20M1320079, https://doi.org/10.1137/ 20M1320079.
- [26] I. TOMINEC AND M. NAZAROV, Residual viscosity stabilized rbf-fd methods for solving nonlinear conservation laws, 2021, https://arxiv.org/abs/2109.07183.
- [27] I. TOMINEC, P.-F. VILLARD, E. LARSSON, V. BAYONA, AND N. CACCIANI, An unfitted radial basis function generated finite difference method applied to thoracic diaphragm simulations, 2021, https://arxiv.org/abs/2103.03673.
- [28] H. Wendland, Piecewise polynomial, positive definite and compactly supported radial functions of minimal degree, Adv. Comput. Math., 4 (1995), pp. 389–396, https://doi.org/10.1007/ BF02123482, https://doi.org/10.1007/BF02123482.
- [29] H. WENDLAND, Fast evaluation of radial basis functions: methods based on partition of unity, in Approximation theory, X (St. Louis, MO, 2001), Innov. Appl. Math., Vanderbilt Univ. Press, Nashville, TN, 2002, pp. 473–483.